

INNATE IMMUNITY

PD-L1 expression on nonclassical monocytes reveals their origin and immunoregulatory function

Mariaelvy Bianchini^{1*}, Johan Duchêne^{1*†}, Donato Santovito¹, Maximilian J. Schloss¹, Maximilien Evrard^{2,3}, Holger Winkels¹, Maria Aslani¹, Sarajo K. Mohanta¹, Michael Horckmans¹, Xavier Blanchet¹, Michael Lacy¹, Philipp von Hundelshausen^{1,4}, Dorothee Atzler^{1,4,5}, Andreas Habenicht¹, Norbert Gerdes⁶, Jaroslav Pelisek⁷, Lai Guan Ng^{2,3}, Sabine Steffens^{1,4}, Christian Weber^{1,8*†}, Remco T. A. Megens^{1,8*}

Copyright © 2019
The Authors, some
rights reserved;
exclusive licensee
American Association
for the Advancement
of Science. No claim
to original U.S.
Government Works

The role of nonclassical monocytes (NCMs) in health and disease is emerging, but their location and function within tissues remain poorly explored. Imaging of NCMs has been limited by the lack of an established single NCM marker. Here, we characterize the immune checkpoint molecule PD-L1 (CD274) as an unequivocal marker for tracking NCMs in circulation and pinpoint their compartmentalized distribution in tissues by two-photon microscopy. Visualization of PD-L1⁺ NCMs in relation to bone marrow vasculature reveals that conversion of classical monocytes into NCMs requires contact with endosteal vessels. Furthermore, PD-L1⁺ NCMs are present in tertiary lymphoid organs (TLOs) under inflammatory conditions in both mice and humans, and NCMs exhibit a PD-L1–dependent immunomodulatory function that promotes T cell apoptosis within TLOs. Our findings establish an unambiguous tool for the investigation of NCMs and shed light on their origin and function.

INTRODUCTION

Monocytes are myeloid cells that circulate through the blood vasculature. In mice, two main subsets of monocytes have been described on the basis of the expression of the surface marker Ly6C and the chemokine receptor CX₃CR1: Ly6C^{high} CX₃CR1⁺ inflammatory/classical monocytes (CMs) and Ly6C^{low} CX₃CR1^{high} patrolling/nonclassical monocytes (NCMs) (1). CMs are recruited at sites of inflammation, where they secrete proinflammatory mediators and become macrophages and dendritic cells upon extravasation, but NCMs have been reported to act as sentinels of the endothelium in the skin (2, 3) and the lung (4) microcirculation. Moreover, it is known that CMs derive from myeloid-committed progenitors in bone marrow (BM) (5–7); however, the origin of NCMs remains unclear. Understanding their behavior, fate, and functions is crucial for elucidating mechanisms of steady-state immune surveillance and pathology and finding ways to potentially target NCMs in inflammatory diseases.

The *Cx3cr1*^{gfp/+} reporter mouse (8) has been instrumental to characterize the patrolling behavior of NCMs in circulation and is a commonly used model for in vivo imaging of NCMs (8–10). To distinguish between CMs and NCMs, this model relies on fluorescence intensity, as CMs express CX₃CR1 at lower levels. This is also true for other CX₃CR1-bearing leukocytes such as macrophages, dendritic cells, natural killer cells, and T cells. Selective depletion of these

populations (2, 11) or exclusion of non-NCM CX₃CR1-bearing cells with complex labeling panels is required to study NCMs in vivo.

Fate mapping studies using constitutive and inducible *Cx3cr1*^{cre} mice revealed that circulating Ly6C^{high} CMs undergo a homeostatic conversion to blood-resident Ly6C^{low} NCMs, thus constituting their obligatory steady-state precursors (12). Conversion involves a differentiation process that depends on the transcription factor CCAAT/enhancer-binding protein beta (C/EBPβ), which leads to down-regulation of Ly6C, and is linked by a transitional differentiation state characterized by Ly6C^{int} intermediate monocytes (IMs) (13). In turn, the expression of CX₃CR1 is increased during conversion. Although first described in the circulation, conversion has also been shown to occur in the BM and spleen (14). In these studies, multi-parameter flow cytometry analysis, in combination with several positive and negative markers, has been instrumental to demonstrate this conversion process. Yet, exploring this phenomenon in situ to determine tissue localization of NCMs with regard to their environment remains challenging. The complex panel of markers used in flow cytometry cannot be directly transferred to optical microscopy, which offers fewer detection channels to discriminate monocyte subsets and is based on subjective signal thresholds. Moreover, a complex combination of markers hampers detection of NCMs in relation to their environment. In this study, we aimed at defining a specific positive marker that would identify NCMs to investigate their origin in steady state and their function in acute inflammatory disease.

RESULTS

In silico identification of candidate markers for NCMs

Using flow cytometry analysis, a sequential gating strategy based on a combination of different markers allows the discrimination of monocyte subsets in peripheral blood (PB) and BM (fig. S1A) (6). To identify a suitable single positive marker for imaging of NCMs, we used an unbiased in silico analysis of the whole NCM and CM transcriptomes by exploiting available open-source databases (fig. S1B). Fifteen genes were identified to be highly expressed by NCMs but

¹Institute for Cardiovascular Prevention, Ludwig-Maximilians-Universität (LMU), 80336 Munich, Germany. ²Singapore Immunology Network (SigN), A*STAR (Agency for Science, Technology and Research), Biopolis, 138648 Singapore. ³School of Biological Sciences, Nanyang Technological University, 637551 Singapore. ⁴German Center for Cardiovascular Research (DZHK), Partner Site Munich Heart Alliance, 80336 Munich, Germany. ⁵Walther Straub Institute of Pharmacology and Toxicology, University of Munich, 80336 Munich, Germany. ⁶Division of Cardiology, Pulmonology, and Vascular Medicine, Medical Faculty, University Hospital Düsseldorf, Düsseldorf, Germany. ⁷Department of Vascular and Endovascular Surgery, Klinikum Rechts der Isar, Technical University of Munich, Munich, Germany. ⁸Cardiovascular Research Institute Maastricht, University of Maastricht, 6229 ER, Maastricht, Netherlands.

*These authors contributed equally to this work.

†Corresponding author. Email: jduchen@med.lmu.de (J.D.); chweber@med.lmu.de (C.W.)

not expressed by CMs in both PB and BM (Fig. 1A, fig. S1C, and data file S1). Only those gene products that localize to the outer cell membrane were considered further for direct labeling with antibodies. Three genes, *Tgfb3*, *Cd274*, and *Pdcd1lg2*, met this criterion (fig. S1C). Of note, *Cx3cr1* and *Spn* (encoding CD43), which are differentially expressed in monocyte subsets (15), were also expressed in CMs and not eligible for consideration (fig. S1D). Because of the broad expression of *Tgfb3* in many cell types (fig. S1E), we excluded it as a candidate. In contrast, the dynamic expression range for *Cd274* [encoding programmed death-ligand 1 (PD-L1)] and *Pdcd1lg2* (encoding CD273/PD-L2) was restricted to few cell types with a marked difference between CMs and NCMs.

PD-L1 marks, distinguishes, and enables tracking of NCMs in PB

To evaluate the suitability of PD-L1 and PD-L2 for selective labeling of circulating NCMs, we assessed their expression levels in all leukocytes by flow cytometry. PD-L2 was not detectable on the surface of monocytes and therefore excluded as a potential marker (fig. S1F). In contrast, PD-L1 demonstrated a strong surface expression on NCMs, whereas CMs did not express it (Fig. 1B). Expression of PD-L1 was also detectable on IMs, albeit substantially lower than on NCMs. All other cell subsets analyzed (neutrophils, eosinophils, CD8⁺ and CD4⁺ T cells, and B cells) did not express PD-L1 (Fig. 1B). To corroborate these findings, we performed confocal microscopy of fluorescently labeled whole blood, which revealed PD-L1⁺CD115⁺ monocytes to be distinguishable from PD-L1⁻CD115⁺ monocytes and Ly6G⁺CD115⁻ polymorphonuclear neutrophils (PMNs) (Fig. 1C).

In addition, comparison of PD-L1⁺ and CX₃CR1^{gfp} cell distribution on t-SNE (unsupervised distributed stochastic neighbor embedding) (16) maps demonstrated that PD-L1 was a preferable marker in terms of specific discrimination of NCMs among all other circulating cell subsets (Fig. 1D and fig. S2A). Specifically, in monocytes, IMs and NCMs were the only cells positive for PD-L1, with NCMs being the most represented population (Fig. 1, E and F, and fig. S2, B and C). By gating on PD-L1 alone (Fig. 1G), the percentage of PD-L1⁺ cells perfectly matched the percentage of NCMs measured with the conventional multiparameter gating strategy (Fig. 1, H and I). By comparison, GFP signals from *Cx3cr1*^{gfp/+} mice and surface CX₃CR1 antibody labeling were less effective to specifically discriminate NCMs (Fig. 1, G, H, and J, and fig. S2E). Moreover, NCMs express high levels of the surface CD43 (15), but flow cytometry analysis demonstrated that CD43 was expressed by other cell types (fig. S3). Furthermore, by analyzing *Nr4a1*-deficient mice, which lack circulating NCMs (fig. S4, A and B) (17), we were able to demonstrate that PD-L1 staining on NCMs was virtually absent in *Nr4a1*^{-/-} mice (fig. S4C).

Next, we questioned whether marking PD-L1 alone in vivo is sufficient for tracking NCMs. After defining optimal conditions (fig. S5), in vivo four-dimensional (4D) two-photon laser scanning microscopy (TPLSM) in microcirculation revealed that PD-L1⁺ cells display characteristic patrolling behavior (Fig. 2, A and B, and movie S1). A detailed analysis (18) of the tracks confirmed a spatially confined patrolling behavior of NCMs at an average speed of 9.9 μm/min (interquartile range, 5.5 to 13.7 μm/min) (Fig. 2, C to F). Together, these results demonstrated the suitability of PD-L1 labeling for studying blood NCMs.

PD-L1 selectively labels NCMs and IMs in the BM

The exact spatial distribution of NCMs in the BM remains unexplored due to the difficulties (i) to detect the low number of NCMs in the

BM (0.25% of all cells), (ii) to discriminate NCMs from other myeloid cells that share some common markers (such as CX₃CR1 also expressed by CMs, macrophages, and myeloid progenitors), and (iii) to transfer multiple fluorescent thresholds used in flow cytometry to microscopy. Thus, we assessed the expression of PD-L1 in BM cells by flow cytometry. Similar to our observations in blood (Fig. 1B), a majority of NCMs and a fraction of IMs exhibited strong PD-L1 expression, whereas no expression was seen on CMs and other BM-resident cells (Fig. 3, A and B). In addition, compared with CX₃CR1 and CD43, PD-L1 was more potent for discriminating BM NCMs (Fig. 3, A to C, and fig. S6, A to D). Next, in whole-mount femur TPLSM imaging, antibody against PD-L1 specifically labeled NCMs or IMs but not CMs and PMNs (Fig. 3, D and E). In addition, no other PD-L1⁺ cell type was detected in this setting (Fig. 3D). By solely using an anti-PD-L1 antibody, we found that PD-L1⁺ cells were enriched in epiphyseal areas compared with diaphysis (Fig. 3, F and G). These data demonstrate that a labeling strategy based on PD-L1 selectively distinguishes NCMs and IMs, thus providing a previously unidentified tool to study the localization and interaction of these cells relative to their environment.

PD-L1⁺ NCMs are enriched in BM regions with higher density of TZ vessels

Given the presence of both CMs and their NCM progenies in the BM, it remains enigmatic how the process of NCM conversion occurs. First, we asked whether the distribution of CMs was also dependent on the BM region. We identified a strong prevalence of CMs over IMs and NCMs (average ratio, 14:1:3) in the diaphysis, whereas the three subsets were more evenly distributed (average ratio, 2:1:2) in the epiphysis (Fig. 4, A and B). Absolute quantification of cell numbers per volume of BM indicated that this altered ratio was due to a substantially higher number of NCMs in the epiphysis, possibly reflecting a conversion from CMs (Fig. 4B). Using specific markers to distinguish BM arterioles (laminin^{high}), transition zone (TZ) vessels (PDGFRβ^{high}), and sinusoids (laminin⁺PDGFRβ⁺) in both epiphysis and diaphysis (Fig. 4C and fig. S7A), we found that PD-L1⁺ cell numbers correlated with the global amount of TZ vessels but not of sinusoids or arterioles (Fig. 4D and table S1). Correlating with the expansion of PD-L1⁺ NCMs, TZ vessels were fivefold more extended in the epiphysis than in the diaphysis (Fig. 4E). We next investigated the spatial relationship between monocyte subsets and TZ vessels. CMs constituted most of the monocytes in physical contact with these vessels, both in epiphysis and diaphysis (Fig. 4F). The relative distance between monocytes and vessels indicated that CMs were also the closest cells to TZ vessels (Fig. 4, G and H, and fig. S7, B and C). In contrast, NCMs were notably distant from TZ vessels, whereas IMs had an intermediate location (Fig. 4, G and H, and fig. S7, B and C). Our findings suggest that a specific vascular environment defines a differential positioning of CMs and NCMs in the BM and that TZ vessels might regulate the conversion of CMs into NCMs.

Conversion of CMs into NCMs in the BM is associated with TZ vessels contact

To address whether TZ vessels are involved in the step-wise conversion of CMs into NCMs via IMs in the BM, we performed adoptive transfer of CMs isolated from CD45.1 donors into CD45.2 recipients (fig. S8A) and imaged the femurs after 24, 48, and 72 hours. These time points were chosen to match with the steady-state conversion

Fig. 1. PD-L1 selectively marks circulating NCMs.

(A) Volcano plot showing gene expression profile in monocyte subsets. Difference of gene expression activity was calculated for each gene. A difference greater than +100% meant that a single gene was highly and only expressed in NCMs. Green box indicates genes that were significantly up-regulated in NCMs ($P < 0.01$; difference $> +100\%$).

(B) PD-L1 expression on blood leukocytes. Representative flow cytometry analysis (left) and quantification (right) of PD-L1 expression from the blood of WT mice. Monocyte subsets were defined as shown in fig. S1A, CMs were $Ly6C^+$, IMs were $Ly6C^{int}$, and NCMs were $Ly6C^-$. Other leukocyte populations ($CD45^+$) were gated as follows: B cells ($CD11b^+$, $B220^+$), CD8 T cells ($CD11b^+$, $B220^-$, $CD8^+$), CD4 T cells ($CD11b^+$, $B220^-$, $CD4^+$), eosinophils ($CD11b^+$, $Ly6G^+$, Ssc^{high}), and neutrophils (PMNs, $CD11b^+$, $CD115^+$, $Ly6G^+$). Data are shown as means \pm SEM. $n = 4$ mice from two independent experiments; $***P < 0.001$.

(C) Representative immunofluorescence confocal micrographs of whole blood stained for PD-L1 (cyan), CD115 (red), and Ly6G (yellow). Scale bar, 20 μm .

(D) Flow cytometry-derived t-SNE reduction maps of whole-blood leukocytes. PD-L1 expression was compared with CX_3CR1 expression from $Cx3cr1^{gfp/+}$ mice. NCMs and CMs are indicated.

(E) Frequency of blood PD-L1⁺ monocyte subsets. Representative flow cytometry analysis (left) and quantification (right) of PD-L1⁺ CMs, IMs, and NCMs from the blood of WT mice. Data are shown as means \pm SEM. $n = 4$ mice from two independent experiments; $***P < 0.001$.

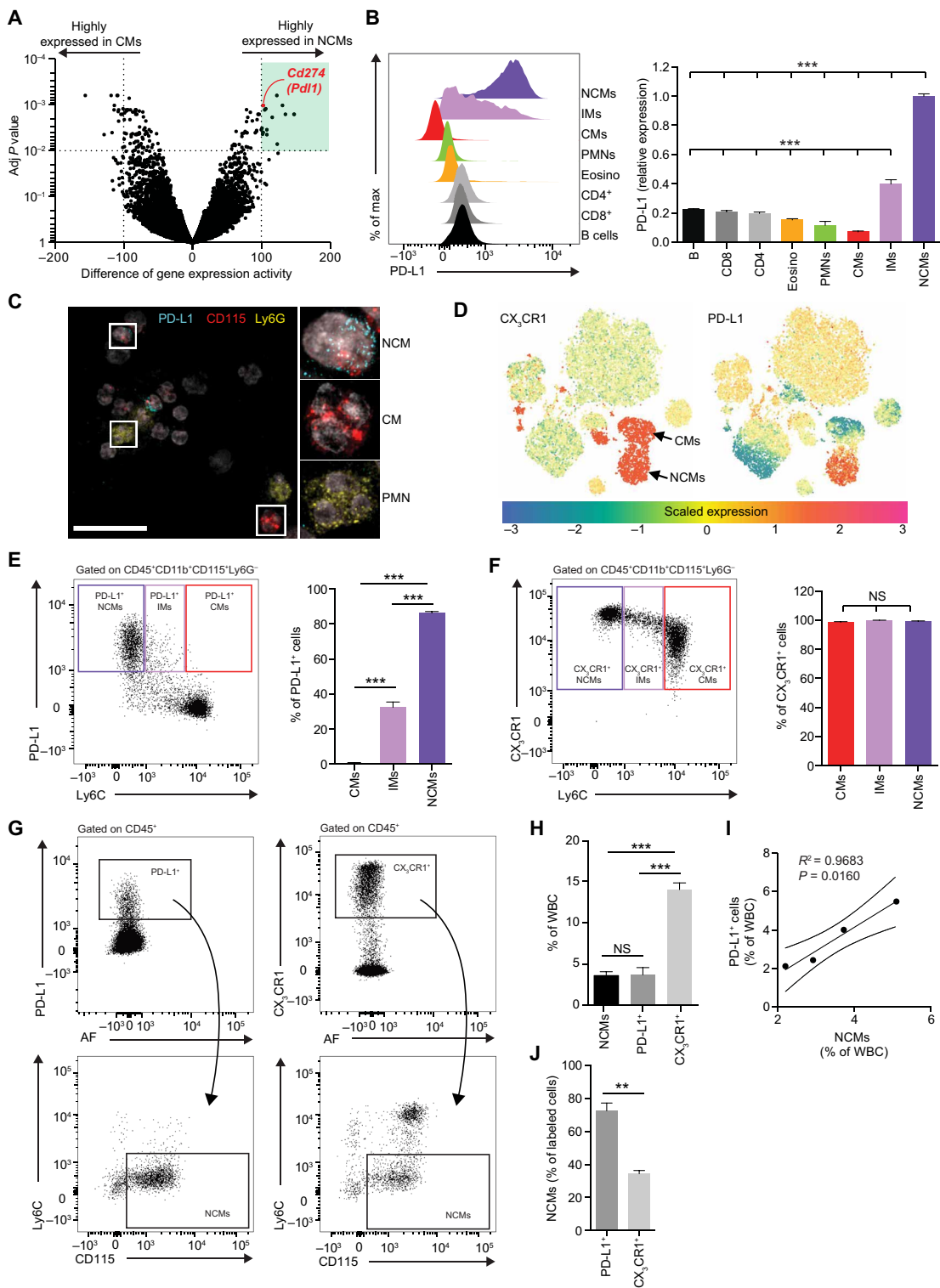
(F) Frequency of blood CX_3CR1^+ monocyte subsets. Representative flow cytometry analysis (left) and quantification (right) of CX_3CR1^+ CMs, IMs, and NCMs from the blood of $Cx3cr1^{gfp/+}$ mice. Data are shown as means \pm SEM. $n = 3$ mice.

(G) Top: Representative flow cytometry analysis comparing gating strategies based on PD-L1 (left) and CX_3CR1 (right) expression. Gates show all PD-L1⁺ and CX_3CR1^+ leukocytes. Bottom: Fraction of NCMs from the parental gates. AF, autofluorescence.

(H) Percentage of PD-L1⁺ and CX_3CR1^+ leukocytes compared with the percentage of NCMs measured by conventional gating strategy (from fig. S1A).

(I) Correlation between percentages of NCMs and PD-L1⁺ leukocytes. WBC, white blood cells.

(J) Quantification of the NCMs fraction in PD-L1⁺ and CX_3CR1^+ leukocytes. Data in (H) and (J) are shown as means \pm SEM. $n = 4$ mice (NCMs and PD-L1) and $n = 3$ mice (CX_3CR1); $**P < 0.01$, $***P < 0.001$. NS, not significant.



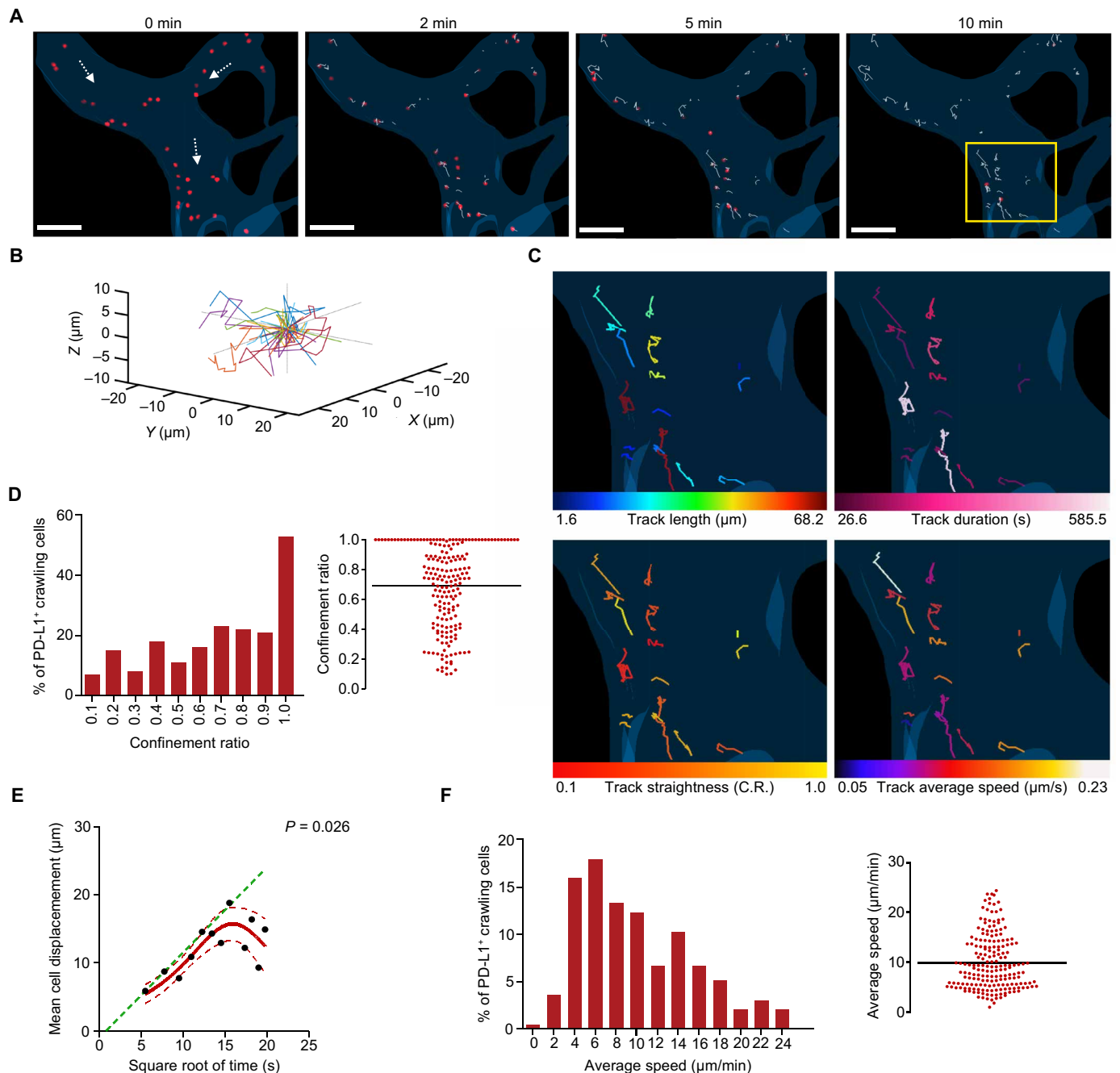


Fig. 2. In vivo tracking of PD-L1⁺ NCMs in the microcirculation. (A) Representative 3D time series showing PD-L1⁺ NCMs (red) crawling in the vasculature of the cremaster muscle. Tracks are shown in white. Vessels were reconstructed on the basis of intrinsic autofluorescent signals (see also movie S1). Arrows show flow direction. Yellow inset is shown in detail in (C). Scale bars, 30 μm . (B) 3D track plot of PD-L1⁺ NCMs from a single 10-min recording showing flow-independent trajectories in all directions. (C) Details from the yellow inset in (A), showing representative cell tracks color-coded according to their length, duration, average speed, and straightness (confinement ratio, C.R.), as depicted. (D to F) Analysis of cell motility. (D) Distribution of PD-L1⁺ NCM confinement ratio and (E) comparison between measured (red line, best fitted curve; see Materials and Methods) and random (green dashed line, predicted by linear regression fitted on the earliest time intervals) mean cell displacement over time. Values are shown as means \pm 95% confidence interval (red dotted lines). (F) Average speed. Lines represent means. All data refer to 195 cells pooled from three independent experiments.

in the BM assessed by a prior bromo-deoxyuridine (BrdU) pulse-chase experiment (fig. S8B). The total number of CD45.1⁺ cells was significantly higher in epiphysis than in diaphysis at all time points (Fig. 5, A and B, and fig. S8C). In both regions, numbers of CD45.1⁺

CMs notably decreased over time, whereas CD45.1⁺ IMs and CD45.1⁺ NCMs peaked at 48 and 72 hours, respectively (Fig. 5C). Further analysis revealed that monocytes in contact with TZ vessels were mainly CD45.1⁺ CMs at all time points (Fig. 5, D to F), whereas the

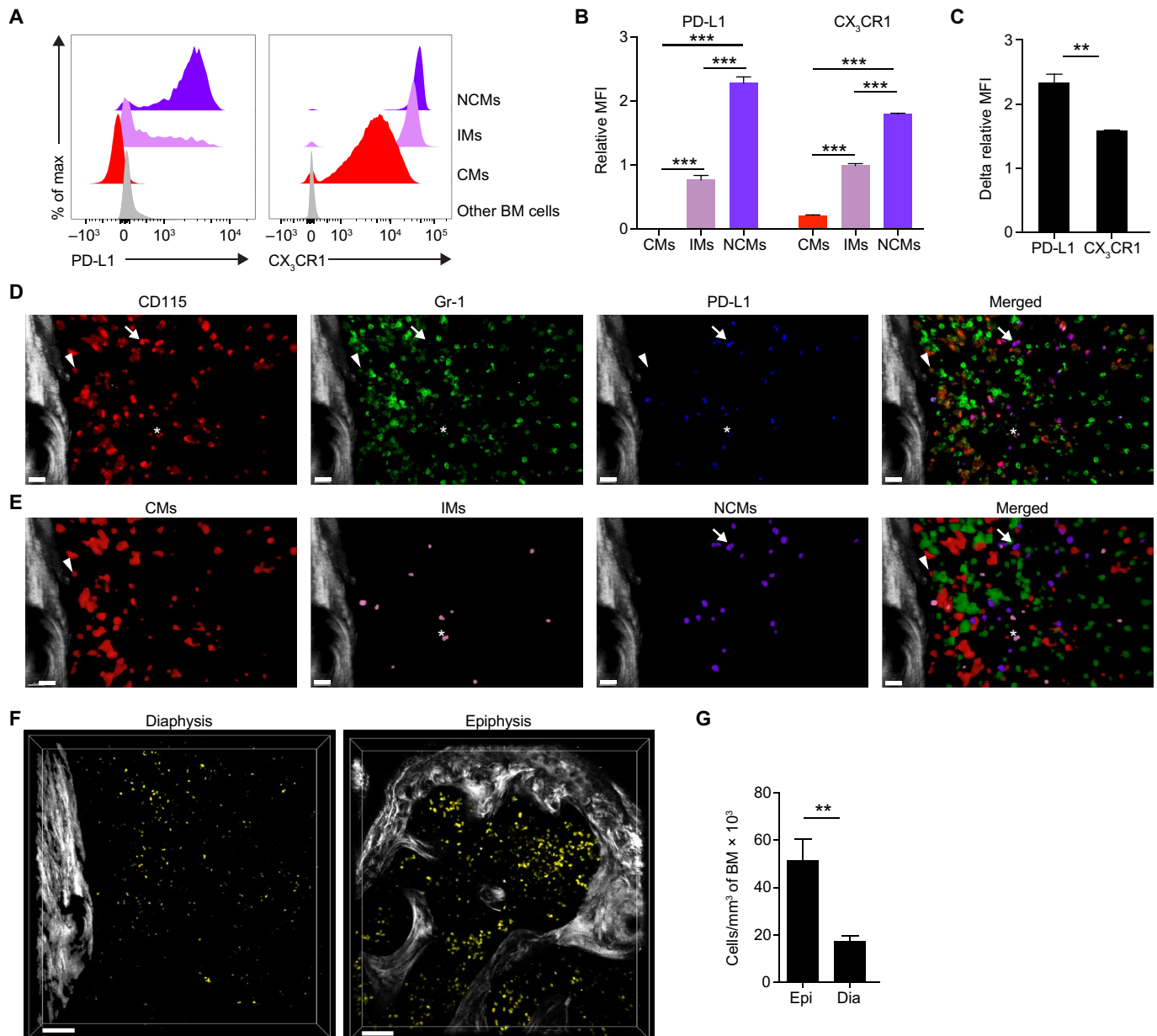


Fig. 3. PD-L1 selectively distinguishes NCMs and IMs in the BM. (A) Representative flow cytometry analysis of PD-L1 and CX₃CR1 expression on BM monocytes from WT and *Cx3cr1^{9fp/+}* mice. Monocyte subsets were gated as shown in Fig. 1A. (B) Quantitative analysis of PD-L1 and CX₃CR1 expression on BM monocyte subsets. Data are shown as means ± SEM. *n* = 4 mice (WT) from two independent experiments and *n* = 3 mice (*Cx3cr1^{9fp/+}* mice); ****P* < 0.001. (C) Difference of PD-L1 and CX₃CR1 mean fluorescent intensity (MFI) between NCMs and CMs. Data are shown as means ± SEM. *n* = 4 mice (WT) from two independent experiments and *n* = 3 (*Cx3cr1^{9fp/+}* mice); ***P* < 0.01. (D) Representative 3D reconstruction of a region in the femoral BM stained for PD-L1 (blue), CD115 (red), and Gr-1 (green). White is bone collagen-derived SHG. Scale bars, 20 μm. (E) 3D segmentation from (D) according to fluorescent color combination (CD115⁻ Gr-1^{high}, PMNs in green; CD115⁺ Gr-1⁻, NCMs in violet; CD115⁺ Gr-1^{low}, IMs in pink; and CD115⁺ Gr-1⁺, CMs in red). Examples of segmented monocyte subsets are indicated by an arrowhead for CM, arrow for NCM, and asterisk for IM. (F) Representative 3D reconstructions of the BM in the femoral epiphysis and diaphysis stained for PD-L1 (yellow). Scale bars, 80 μm. (G) Absolute quantification of PD-L1⁺ cells in epiphysis (Epi) and diaphysis (Dia). Data are shown as means ± SEM. *n* = 4 mice. ***P* < 0.01.

proportion of CD45.1⁺ IMs increased transiently at 48 hours (Fig. 5E). Moreover, the distance index of cells relative to the vessels showed that the number of IMs and NCMs in the sinusoid compartment increased at 48 and 72 hours, respectively (Fig. 5F), suggesting that monocytes move from TZ vessels toward the sinusoids during their conversion. Together, these findings provide a spatiotemporal representation of monocytes conversion in relation to BM vessels.

Altered TZ vessels is associated with defective conversion of CMs into NCMs in aged mice

Aging is associated with a loss of structure and function of TZ vessels in the BM (19), and we hypothesized that CM-to-NCM conversion may be altered in aged mice. We found that circulating CMs, but not IMs or NCMs, were increased in aged mice (Fig. 6, A to C). TPLSM of the BM showed that the distribution of monocytes was

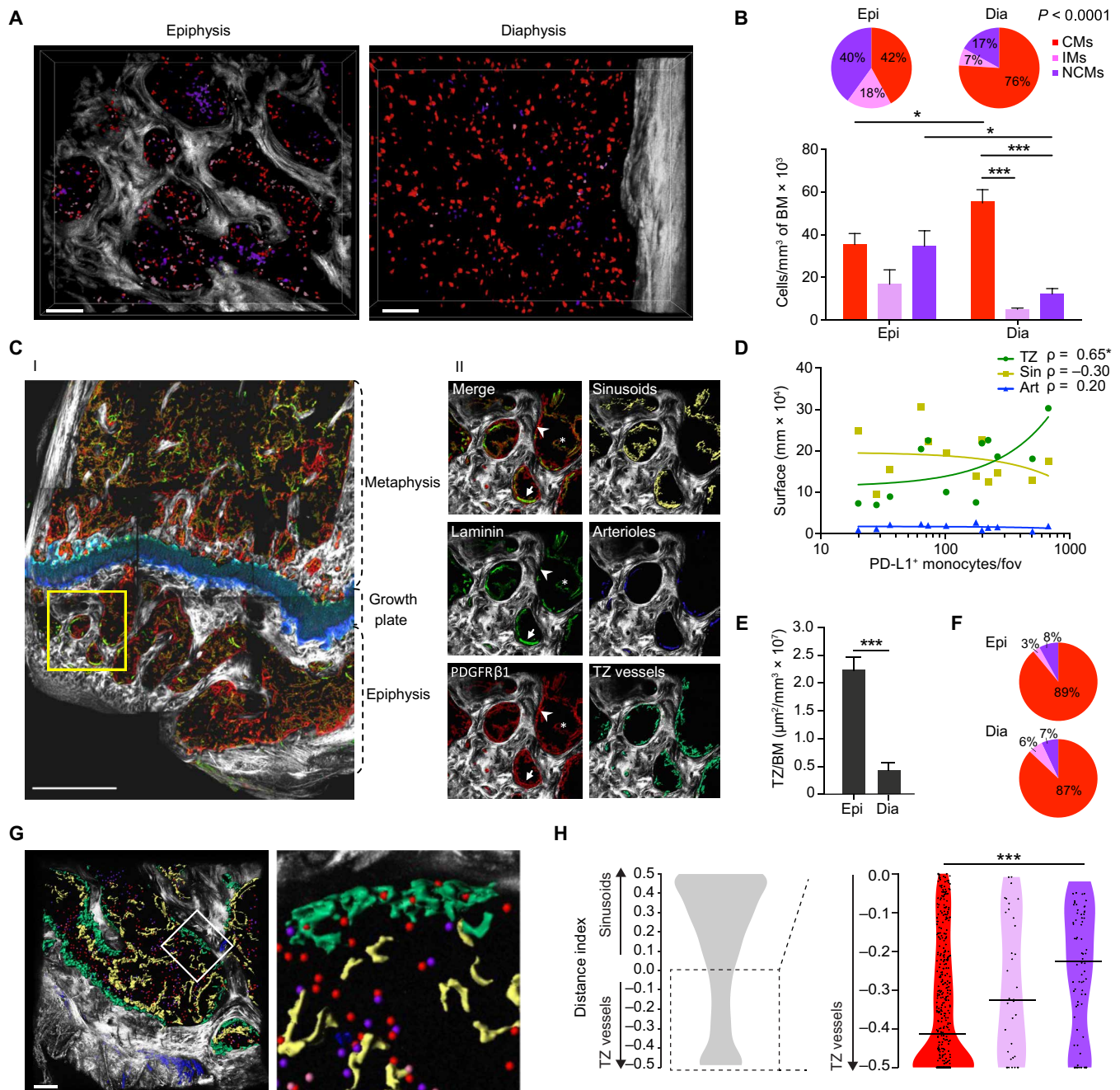


Fig. 4. PD-L1⁺NCMs are enriched in BM regions with higher density of TZ vessels. (A) Representative 3D reconstructions of BM monocytes in the femoral epiphysis and diaphysis. Monocytes (CD115⁺) were classified after segmentation based on the expression of PD-L1 and Gr-1. CMs (red), IMs (pink), and NCMs (violet). Scale bars, 80 μm. (B) Distribution of monocyte subsets in epiphysis and diaphysis. Percentage (top) and absolute quantification (bottom) of monocyte subsets. Values are expressed as means (top) and means ± SEM (bottom). Data are representative of four independent experiments. * $P < 0.05$, *** $P < 0.001$. (C) Representative micrograph of the femoral vessel architecture in distal epiphysis and metaphysis. Whole-mounted femur was stained for laminin (green), and PDGFRβ1 (red) and stitched maximum intensity projection was generated (I). Inset is magnified on the right. (II) Merge and single channels are shown, as well as the 3D surface reconstruction of sinusoids (asterisk, laminin⁺PDGFRβ1⁺), arterioles (arrow, laminin^{bright}PDGFRβ1⁻), and TZ vessels (arrowhead, laminin⁻PDGFRβ1^{bright}). Scale bar, 500 μm. (D) Correlation between the number of PD-L1⁺ monocytes (IMs and NCMs) and the surface of TZ vessels, sinusoids, and arterioles. Data were collected from 12 random areas of the femur deriving from four independent experiments. Spearman's coefficients are indicated; * $P < 0.05$, fov, field of view. (E) Ratio between the TZ vessel surface and BM volume in epiphysis and diaphysis. Data are shown as means ± SEM. $n = 6$ fov from three mice. *** $P < 0.001$. (F) Percentage of CMs, IMs, and NCMs among monocytes in contact with TZ vessels in epiphysis and diaphysis. Data refer to 231 (epiphysis) and 137 (diaphysis) cells from two independent experiments. (G) Representative 3D reconstruction showing monocyte subsets and vessels in the epiphysis. CMs (red spheres), IMs (pink spheres), and NCMs (violet spheres). Sinusoids (yellow) and TZ vessels (green). Inset is magnified on the right. Scale bar, 80 μm. (H) Distance index of epiphyseal monocyte subsets. Left: Distance index of all monocytes to the closest sinusoid and TZ vessel. Right: Distance index of CMs, IMs, and NCMs closest to the TZ vessels. In the violin plots, center lines represent the median, and dots represent cells. $n = 1955$ monocytes (left); $n = 470$ CMs, $n = 35$ IMs, and $n = 79$ NCMs (right) from two independent experiments.

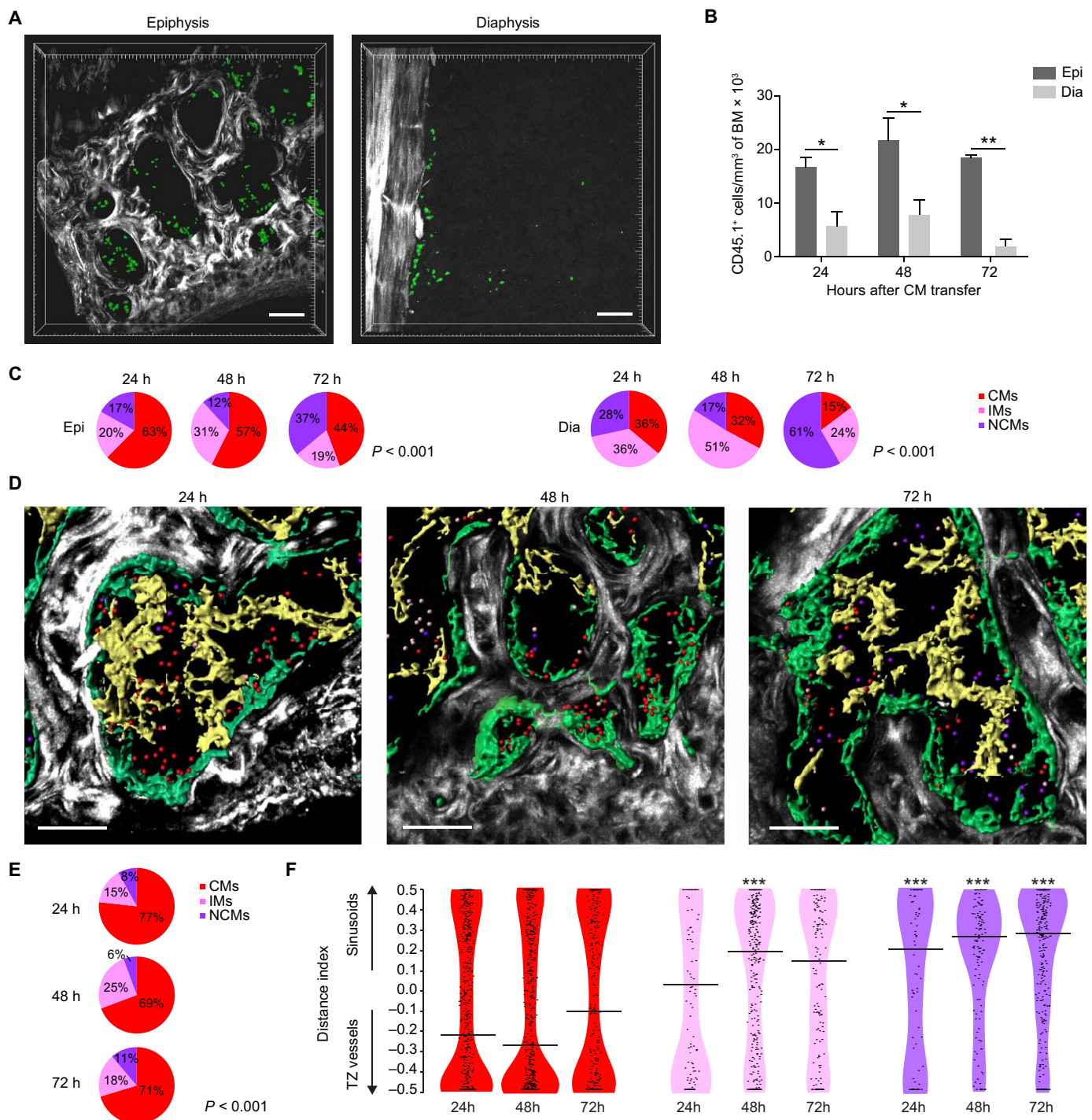


Fig. 5. Spatiotemporal analysis of monocyte conversion in the BM. (A to F) Conversion assessed by TPLSM imaging of the BM after adoptive transfer of CD45.1⁺ CMs into CD45.2 recipient. (A) Representative 3D reconstructions of CD45.1⁺ donor-derived monocytes (green) in epiphysis and diaphysis of CD45.2 recipient mice 24 hours after transfer of CMs. Scale bars, 80 μ m. (B) Absolute quantification of CD45.1⁺ donor-derived monocytes in the epiphysis and diaphysis of CD45.2 recipient mice 24, 48, and 72 hours after transfer of CMs. Data are shown as means \pm SEM. $n = 2$ mice per time point. * $P < 0.05$, ** $P < 0.01$. (C) Percentage of CD45.1⁺ monocyte subsets in the epiphysis and diaphysis 24, 48, and 72 hours after adoptive transfer. $n = 2$ mice per time point. (D) Representative 3D reconstructions of epiphyseal regions showing the position of CMs (red spheres), IMs (pink spheres), and NCMs (violet spheres) in relation to sinusoids (yellow) and TZ vessels (green) 24, 48, and 72 hours after transfer. Scale bars, 80 μ m. (E) Percentage of monocyte subsets among CD45.1⁺ monocytes in contact with TZ vessels at all time points after adoptive transfer. $n = 2$ mice per time point. (F) Distance index of CD45.1⁺ CMs, IMs, and NCMs to the closest sinusoid and TZ vessel at the indicated time points after transfer. In the violin plots, center lines represent the median, and dots represent cells. $n = 656, 723,$ and 344 CMs, $n = 246, 360,$ and 154 IMs, and $n = 211, 145,$ and 271 NCMs are pooled from two mice per time point.

markedly altered in the epiphysis of these mice (Fig. 6, D and E). Absolute quantification indicated that this was due to a marked reduction in the number of NCMs (Fig. 6, D and F), whereas the number of CMs was substantially increased (Fig. 6, D and G). This was associated with a paucity of PDGFR β^{high} TZ vessels (Fig. 6, D and H). Hence, the application of PD-L1 to mark NCMs in a mouse model of aging enabled us to further substantiate a potential role of TZ vessels in promoting the conversion of CMs into NCMs in the BM.

PD-L1 identifies NCMs in tertiary lymphoid organs

Next, we tested whether PD-L1 could be used to study NCMs under inflammatory conditions. In a mouse model of myocardial infarction (MI), NCMs remained the only circulating cells displaying a detectable expression of the marker (Fig. 7, A and B). Immune responses to tissue damage in MI are coordinated by tertiary lymphoid organs (TLOs) in the pericardial adipose tissue (PAT) (20), where B and T cells expand shortly after the onset of MI. NCMs also accumulated in PAT after MI (Fig. 7C) and maintained a markedly higher expression of PD-L1 than other leukocytes (Fig. 7D and fig. S9, A to C). Using TPLSM, we found that monocytes clustered in TLOs (Fig. 7E) and that NCMs could be specifically identified as CD115 $^+$ PD-L1 $^+$ cells (Fig. 7F). Moreover, all PD-L1 $^+$ NCMs were found in the core of the TLOs, but some of them were still in contact with the vasculature (Fig. 7G and fig. S9D), suggesting that NCMs were actively recruited into TLOs during MI. PD-L1 expression by CD14 $^{\text{dim}}$ CD16 $^+$ NCMs was also detected in human TLOs of patients with cardiovascular disease, namely, abdominal aortic aneurysm (Fig. 7H and fig. S9E). Collectively, these results establish PD-L1 as a reliable marker for NCMs under inflammatory conditions.

NCMs regulate T cell survival in TLOs via PD-L1

PD-L1 is a checkpoint regulator of the adaptive immune response as it can induce T cell anergy, cytostasis, and apoptosis (21). Hence, we verified whether PD-L1 expressed by NCMs could also regulate the adaptive immune response in TLOs. Three days after MI, numbers of PD-L1 $^+$ NCMs were significantly increased in TLOs (Fig. 8, A and B). Moreover, a notable fraction of NCMs established cell-cell contacts with T cells (Fig. 8C). Because PD-L1 was positioned at the interface between NCMs and T cells (Fig. 8D), we postulated that PD-L1 could be involved in cell juxtaposition. Blocking PD-L1 in vivo (fig. S10A) resulted in a significant decrease of NCMs in contact with T cells 3 days after MI (Fig. 8, E and F). Anti-PD-L1 treatment did not affect the total number of NCMs in TLOs (Fig. 8G) or in circulation (fig. S10B). Moreover, although the numbers of T cells in TLOs decreased over time after MI in controls, this effect was abrogated in mice treated with the anti-PD-L1 antibody (Fig. 8H) and was associated with a reduction of Annexin V $^+$ T cells undergoing apoptosis (Fig. 8, I and J). Together, these results suggest that PD-L1 expressed by NCMs regulates T cell survival in TLOs.

DISCUSSION

Patrolling behavior of Ly6C $^{\text{low}}$ NCMs in the microcirculation has first been described by Geissmann and colleagues (2). Since then, several efforts have been made to study their function in different tissues and organs under steady-state conditions, as well as in disease models directly or indirectly involving the vasculature (10, 22). The imaging of NCMs has relied on reporter mice expressing green fluorescent protein (GFP) under the control of the *Cx3cr1* promoter

(8). Although undoubtedly useful to reveal several key aspects of NCM biology, this tool has limitations. We and others have found that *Cx3cr1* $^{\text{GFP/+}}$ mice do not uniquely label NCMs in both circulation and tissues (5, 6, 11). This is not entirely unexpected, as this reporter mouse model was originally developed to visualize the whole monocyte compartment including Ly6C $^{\text{high}}$ CMs, which constitute about 50% of all circulating monocytes (8). Moreover, other cell types also express CX $_3$ CR1, which requires their depletion (2, 11) or selective exclusion.

Under these premises, the development of a selective mouse strain-independent labeling strategy for cell detection is desirable. We aimed to identify an NCM-specific surface marker that can be exploited for fluorescent antibody-based cell labeling. Here, we report that PD-L1 is expressed by NCMs in PB and BM. Whereas PD-L1 expression on cancer cells has been described (23), its expression by PB and BM NCMs has been less well studied. We could also demonstrate that targeting PD-L1 is sufficiently specific and sensitive to accomplish in vivo tracking of NCMs by 3D TPLSM over prolonged periods without affecting cell behavior. NCM motility parameters obtained in the microvasculature were consistent with data reported in the literature using GFP-reporter mice deficient in lymphoid and natural killer cells (2). This is in line with other antibodies used to track leukocyte subsets (e.g., Ly6G, CD4, or CD8), which also do not perturb cell behavior when used at similar amounts (24, 25). Hence, PD-L1 antibody labeling provides a robust method for studying NCMs, which ultimately extends the existing arsenal of tools commonly used for studying these cells. As antibodies can be conjugated to a variety of contrast agents other than fluorophores, anti-PD-L1 immune labeling holds the potential for detection of NCMs with other imaging technologies.

The concept of monocyte subset interdependence has only emerged recently when it was shown that CMs can convert to NCMs through IMs in the bloodstream (12, 13) and other organs (14). Targeting of PD-L1 offered a unique opportunity for specifically visualizing NCMs with a single marker, an advantageous criterion for in situ analysis and studies that explore location in relation to other monocyte subsets and BM vasculature in a single whole-mounted BM specimen. We exploited the specificity of PD-L1 expression by NCMs to uncover a blood vessel-dependent microenvironment for monocyte conversion in the BM. Most of the monocytes in the diaphysis were CMs, but unexpectedly, NCMs were enriched in the epiphysis. A possible explanation for this enrichment might be that the epiphysis is a more specialized environment for the production, storage, or homing of NCMs. Epiphysis/metaphysis and diaphysis were previously described to harbor different kind of blood vessels (26, 27). Whereas arterioles run from the central cavity of the diaphysis and branch toward the trabecular bone to supply oxygen and nutrients, sinusoids occupy the central area of each bone cavity, converge into the central vein, and constitute the main cell entrance and exit route to and from the BM (28). TZ vessels connect both the arteriolar and sinusoidal district and extend along the endosteal regions; as a consequence, their presence is particularly abundant at the trabecular bone of the metaphysis and epiphysis (Fig. 4C) (19, 29). We correlated NCM and IM numbers to the presence of TZ vessels and observed a gradient of distribution of monocyte subsets from TZ vessels toward sinusoids. In combination with CM transfer experiments, whole-mount imaging of the BM indicated that monocyte conversion occurs in particular areas characterized by a prominent presence of TZ vessels. In addition, the conversion from CM to NCM was less

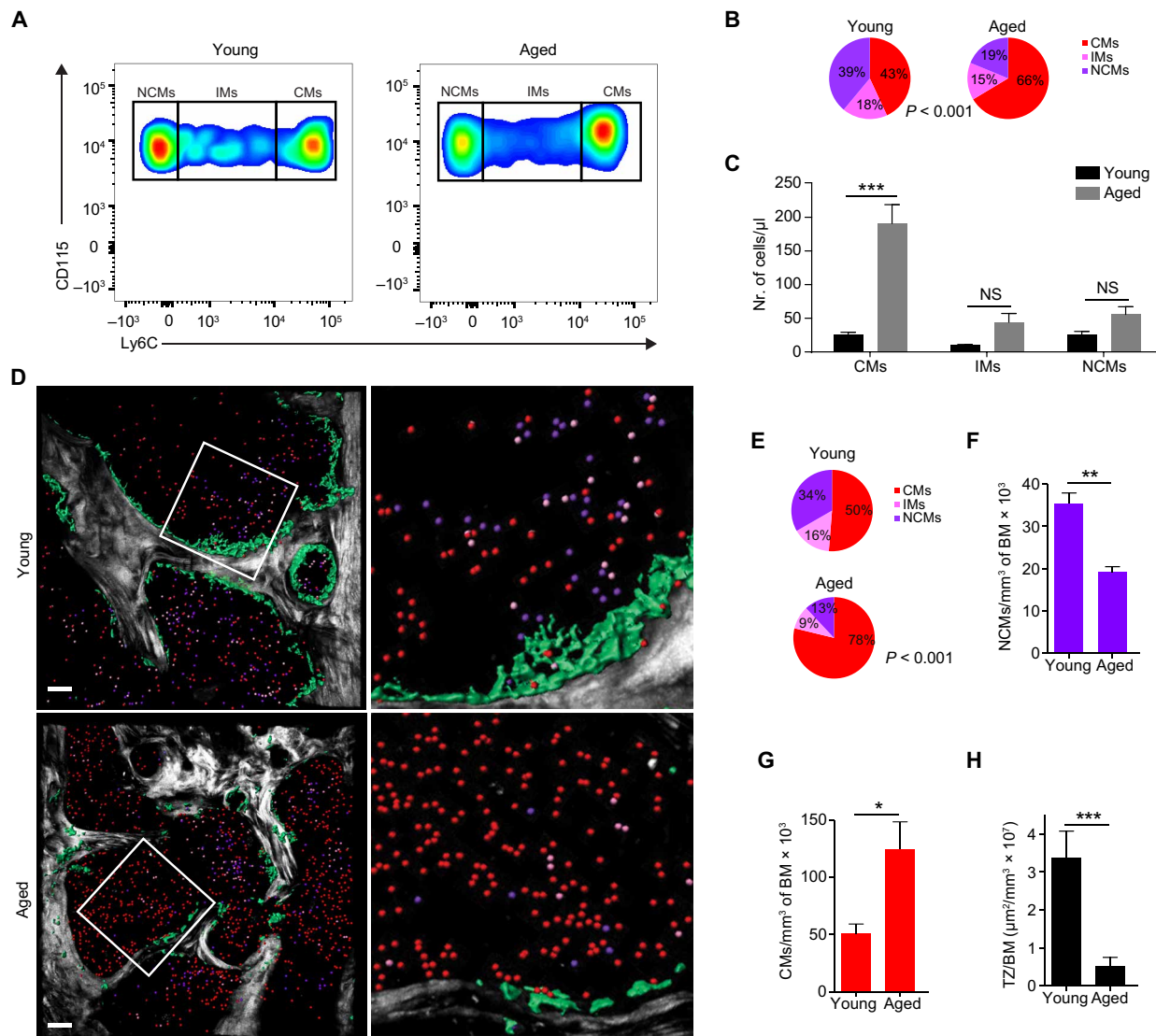


Fig. 6. Conversion of CMs into NCMs is defective in the BM of aged mice. (A) Representative flow cytometry analysis, (B) percentages, and (C) absolute counts of monocyte subpopulations in the blood of young and aged mice. Data are shown as means (B) and means \pm SEM (C). $n = 8$ (young) and 7 (aged) mice from three independent experiments. $***P < 0.001$. (D) Representative 3D reconstructions of epiphyseal regions showing CMs (red spheres), IMs (pink spheres), and NCMs (violet spheres) as well as TZ vessels (green) in young and aged mice. White insets are tilted and shown in detail on the left. Scale bars, 80 μ m. (E) Percentages of monocyte subsets in the epiphysis of young and aged mice. Data are shown as means of four mice. (F) Absolute quantification of NCMs in epiphysis of young and aged mice. Data are shown as means \pm SEM. $n = 4$ mice per group. $**P < 0.01$. (G) Absolute quantification of CMs in epiphysis of young and aged mice. Data are shown as means \pm SEM. $n = 4$ mice per group. $*P < 0.05$. (H) Ratio between the TZ vessel surface and BM volume in epiphysis of young and aged mice. Data are shown as means \pm SEM. $n = 10$ fov from four mice. $***P < 0.001$.

efficient in aged mice, which harbor TZ vessels with an altered structure and function, further indicating a pivotal role of TZ vessels in the conversion process. Together, our data suggest that preferential homing of circulating CMs to the epiphysis and/or their prolonged presence in that area will drive their transition to NCMs after an interaction with TZ vessels. As a caveat, our current data only allow us to speculate about the molecular triggers involved in the conversion process. The TZ vessels lining the endosteum are considered to be crucial for maintaining the hematopoietic niche, as they promote hematopoietic stem cell proliferation through Notch signaling (19). The Notch pathway has also been implicated in the regulation of CM-to-NCM transitioning by endothelial cells in vitro, and its ligand DLL-1 was found to be

expressed by a subset of blood vessels in both the spleen and BM, although the vessel morphology has not been precisely detailed (14). A more extensive characterization of the molecular determinants expressed by TZ vessels, as well as a deeper insight into the cellular and biochemical microenvironment of their immediate vicinity, might provide additional clues for understanding how monocyte fate is locally regulated.

Monocytes are key innate immune cells that regulate homeostatic surveillance and inflammatory diseases. Whereas CMs have been extensively investigated (30), NCMs remain less well studied. So far, research has largely focused on the role of NCMs as early responders to tissue damage and promoters of neutrophil recruitment or on

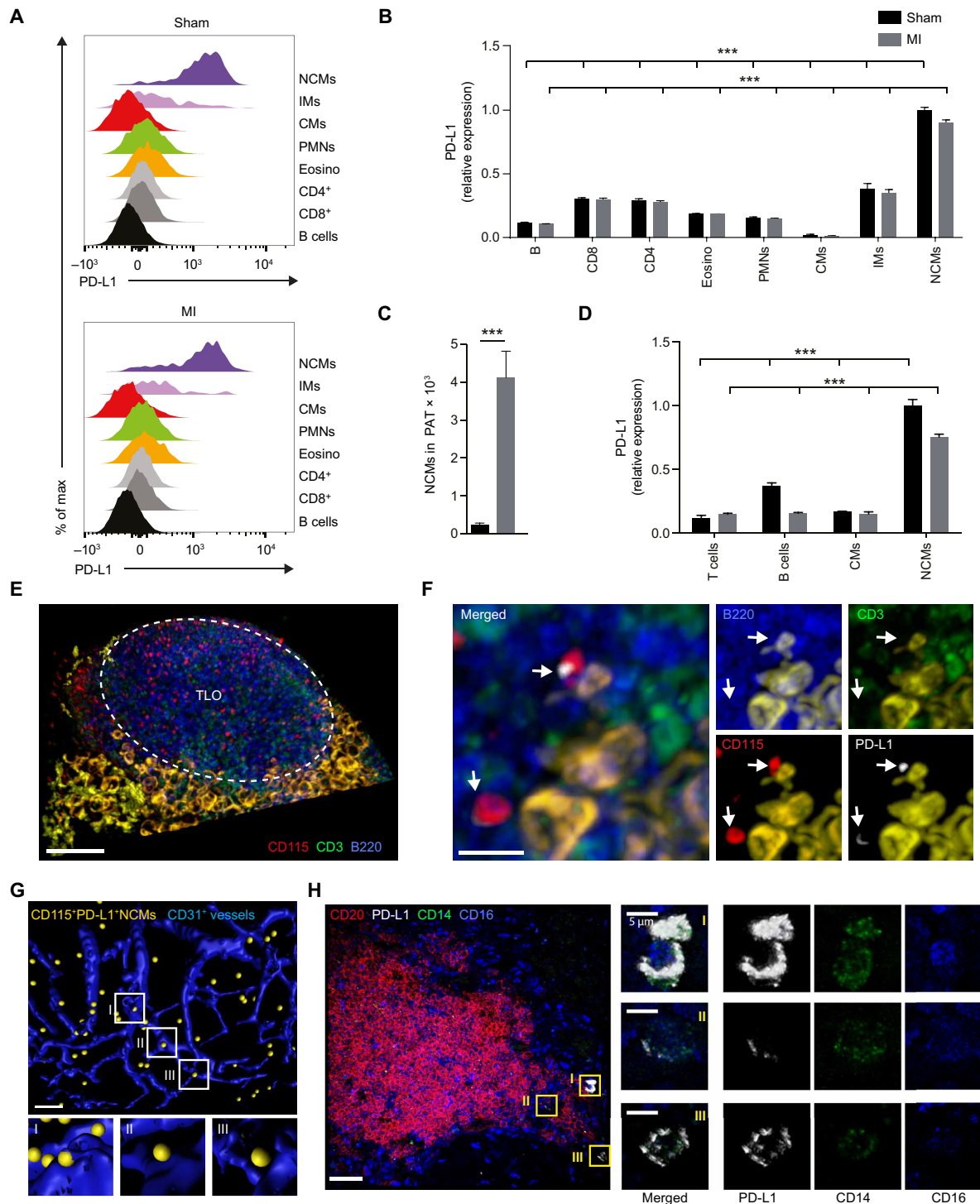


Fig. 7. PD-L1 expression is maintained on NCMs under inflammatory conditions and PD-L1⁺ NCMs are found in TLOs. (A) Representative flow cytometry and (B) quantification of PD-L1 expression on blood leukocytes in mice after sham or MI surgery. Data are shown as means \pm SEM. $n = 3$ (sham) and $n = 6$ (MI) mice. *** $P < 0.001$. (C) Quantification of NCMs in PAT of mice after sham or MI surgery. Data are shown as means \pm SEM. $n = 5$. *** $P < 0.001$. (D) Quantification of PD-L1 expression on leukocyte populations in PAT of mice after sham or MI surgery. Data are shown as means \pm SEM. $n = 3$. *** $P < 0.001$. (E) Representative 3D TPLSM reconstruction of a TLO in PAT of mice showing clustered B cells (B220⁺, blue), T cells (CD3⁺, green), and monocytes (CD115⁺, red). Adipocyte-derived autofluorescence is depicted in yellow. Scale bar, 90 μ m. (F) Detailed TPLSM micrograph of PD-L1⁺ (white), CD115⁺ (red) NCMs (indicated by the arrows), B220⁺ (blue) B cells, and CD3⁺ (green) T cells in a TLO in PAT of mice. Single markers are shown on the right. Adipocyte-derived autofluorescence is depicted in yellow. Scale bar, 20 μ m. (G) Representative 3D TPLSM reconstruction of CD115⁺ PD-L1⁺ NCMs (yellow spheres) and CD31⁺ blood vessels (blue) in a TLO of PAT. Three examples of NCMs in contact with the extraluminal side of the vascular wall (tilted insets) are shown in detail. Scale bar, 30 μ m. (H) Confocal laser scanning microscopy (CLSM) image of a TLO in human adventitial fat of the aorta, showing CD20⁺ (red) B cells and PD-L1⁺ (white), CD14⁺ (green), CD16⁺ (blue) NCMs. Representative PD-L1⁺ NCMs are indicated by Roman numerals and shown in detail as single-color micrographs on the right. Scale bars, 20 μ m and 5 μ m.

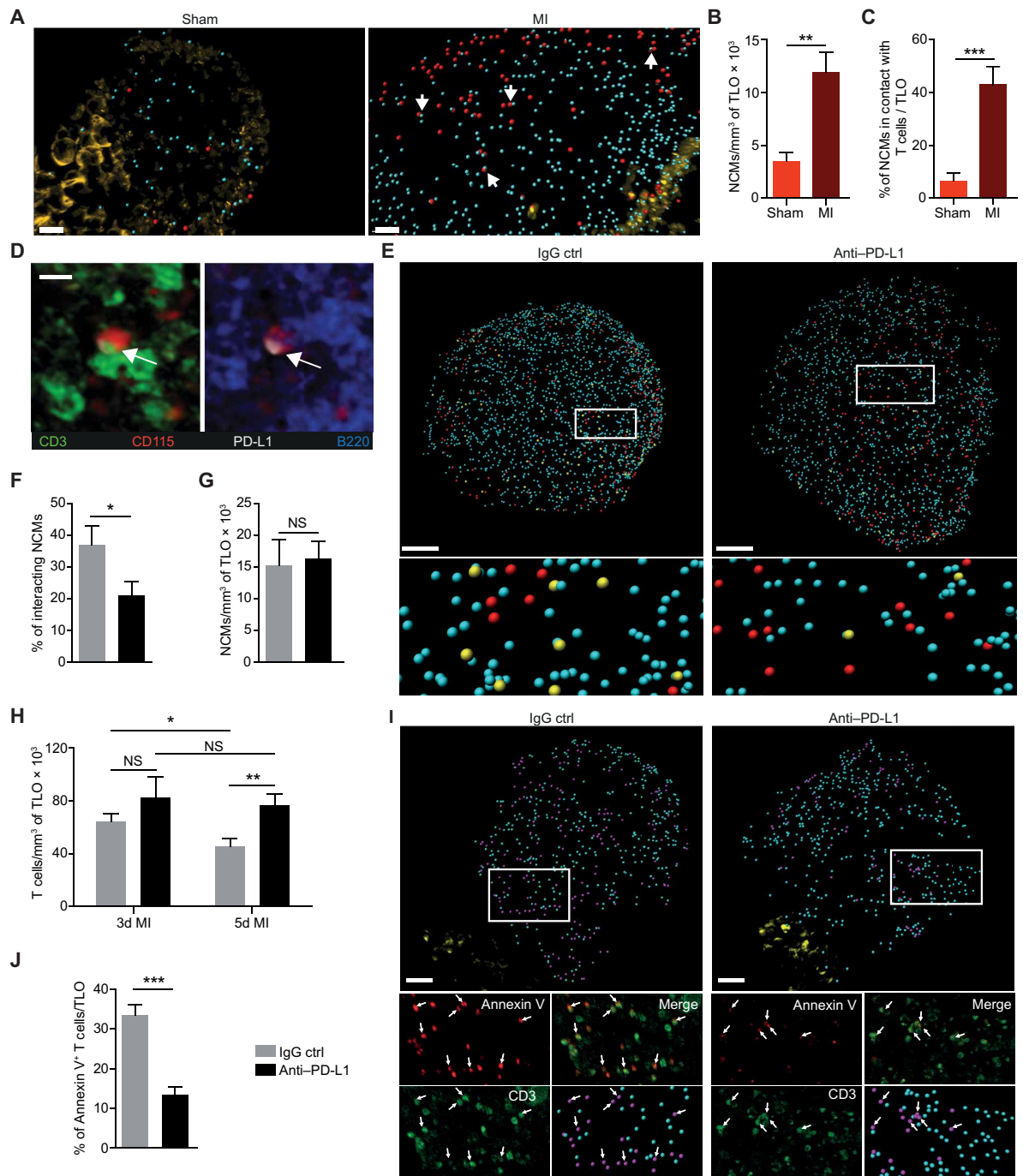


Fig. 8. NCMs regulate T cell survival in TLOs via PD-L1. (A to C) Increase of NCM–T cell contacts in TLOs in the PAT of mice 3 days after MI. (A) Representative TPLSM 3D reconstruction of PD-L1⁺ NCMs (red spheres) and T cells (cyan spheres) after MI (right) or sham (left) surgery. Examples of NCM–T cell contacts are indicated by the arrows. Scale bars, 30 μ m. (B) TPLSM-derived quantification of PD-L1⁺ NCMs normalized on volume of TLOs. Data are shown as means \pm SEM. $n = 8$ (sham) and $n = 10$ (MI) TLOs from three to five mice, respectively. $**P < 0.01$. (C) Percentage of PD-L1⁺ NCMs in direct contact with T cells in single TLOs. Data are shown as mean \pm SEM. $n = 9$ (sham) and $n = 10$ (MI) TLOs from three to five mice, respectively. $***P < 0.001$. (D) Representative single-plane TPLSM micrograph of a PD-L1⁺ (white) CD115⁺ (red) NCM in contact with CD3⁺ (green) T cells and B220⁺ (blue) B cells. PD-L1 at the NCM–T cell interface is indicated by the arrow. Scale bar, 10 μ m. (E to J) Effect of treatment with control IgG or the anti-PD-L1 antibody on NCMs and T cells in TLOs of mice 3 days after MI. (E) Representative TPLSM reconstructions of CD115⁺ Ly6C⁻ NCMs (red spheres) and T cell (cyan spheres). NCMs in direct contact with T cells are depicted as yellow spheres. Insets are shown in detail at the bottom. Scale bars, 80 μ m. (F) Percentage of CD115⁺ Ly6C⁻ NCMs in direct contact with T cells. Data are shown as means \pm SEM. $n = 7$ (sham) and $n = 9$ (MI) TLOs from three mice per group. $*P < 0.05$. (G) Absolute quantification of CD115⁺ Ly6C⁻ NCMs per volume of TLOs. Data are shown as means \pm SEM. $n = 7$ (sham) and $n = 9$ (MI) TLOs from three mice per group. (H) Absolute quantification of T cells in single TLOs in the PAT of mice 3 days (3d; left) and 5 days (right) after MI and treatment. Data are shown as means \pm SEM. $n > 11$ TLOs from three to four mice per group. $*P < 0.05$, $**P < 0.01$. (I) Representative TPLSM reconstructions of Annexin V⁺ (pink spheres) and Annexin V⁻ (cyan spheres) T cells after treatment. Insets are shown in detail and as single colors at the bottom. Scale bars, 80 μ m. (J) Percentage of Annexin V⁺ T cells in single TLOs 3 days after MI. Data are shown as means \pm SEM. $n > 11$ TLOs from three to four mice per group. $***P < 0.001$.

their function as scavengers of debris in vessels and tissues (3, 22). In the present study, we provide evidence that PD-L1 expression is maintained on mouse NCMs and can be detected in human NCMs in the course of the inflammatory response during cardiovascular disease. Together with the discovery that PD-L1 is actively used by NCMs to regulate T cell expansion in TLOs, our work further indicates that NCMs may be involved in the pathogenesis of chronic disorders that are associated with the presence and development of TLOs, including cardiovascular disease (20) and tumors (31). Recent studies have described the acquisition of a PD-L1⁺ phenotype by human monocytes in the context of lymphoid malignancies (32, 33). PD-L1 is a key target of immune checkpoint blocking strategies used for cancer therapy (21). PD-L1 may also be expressed by some cancer cells, e.g., in the circulation (34). In this context, PD-L1 could be used in combination with a monocyte marker, as used herein, to discriminate NCMs from cancer cells. To our knowledge, the potential impact of anti-PD-L1 regimens on NCMs at present has been disregarded in both mouse models and clinical trials, however, might now warrant further investigation.

Overall, our study not only establishes PD-L1 as a tool to track NCMs but also pinpoints a local site for their production in the BM and a regulatory role in TLOs. Hence, PD-L1 paves the way for a better understanding of NCM dynamics in steady state, aging, and disease.

MATERIALS AND METHODS

Study design

The objectives of the present study were to identify a robust and specific marker for the microscopic identification of mouse NCMs in vivo/in situ and to prove its usefulness in a proof-of-concept application relevant to the field of NCM biology. Detailed spatio-temporal description of monocyte conversion in the BM and investigation of PD-L1 function on NCMs were pursued after initial data analysis. Bioinformatics data were collected from and analyzed with open-source databases (GEO, GEXC, and DAVID). Controlled laboratory animal experiments were conducted on wild-type (WT) and transgenic mice (*Cx3cr1*^{gfp/+} and *Nr4a1*^{-/-}), without blinding or randomization, and included in vivo manipulation (imaging, surgery, antibody-based inhibitory treatment, and cell transfer) and tissue collection (blood, BM, and PAT) for ex vivo methodologies. Human data were generated on surgical aortic samples of patients collected with informed consent (35). Relevant technical procedures included flow cytometry and 3D and 4D TPLSM, followed by sophisticated computational image analysis.

Animal models

C57BL/6J, CD45.1, CD45.2, *Cx3cr1*^{gfp/+}, and *Nr4a1*^{-/-} mice were purchased from the Jackson Laboratory (Bar Harbor, USA). For all ex vivo experimental procedures, 8- to 12-week-old females or males and 78-week-old males were used. For in vivo imaging of the cremaster muscle, 12-week-old males were used. Animals were housed in pathogen-free animal facilities at the Ludwig-Maximilians-Universität of Munich (Germany) and at the Biological Resource Centre of A*STAR (Singapore). All procedures were approved by the Government of Upper Bavaria, Munich, Germany, in compliance with German and European Union guidelines, and by the Institutional Animal Care and Use Committee of the BRC, Singapore.

For blood collection and in vivo imaging, mice were anesthetized with an intraperitoneal injection of ketamine (120 mg/kg) and xylazine

(8 mg/kg) in saline. For femur and PAT collection, mice were euthanized by cervical dislocation. For MI model, mice were anesthetized with midazolam (5 mg/kg), medetomidin (0.5 mg/kg), and fentanyl (0.05 mg/kg), intubated, and ventilated with a MiniVent mouse ventilator (Harvard Apparatus, Holliston, MA).

Tissue flow cytometry

Blood was withdrawn from the heart and collected in EDTA-precoated tubes. Erythrocyte lysis was performed by mixing whole blood 1:10 with ammonium-chloride-potassium (ACK) buffer for 10 min at room temperature (RT). BM was flushed via centrifugation (8600g for 1 min) of the femurs after exposure of the distal metaphysis and resuspended into fluorescence-activated cell sorting (FACS) buffer [phosphate-buffered saline (PBS) and 0.1% bovine serum albumin (BSA)]. PAT was washed into PBS, minced, and digested with collagenase I (450 U/ml), collagenase XI (125 U/ml), hyaluronidase type I-S (60 U/ml), and deoxyribonuclease (60 U/ml) at 37°C for 1 hour. Cell lysates were filtered through a 100- μ m nylon mesh strainer and centrifuged at 500g for 10 min at 4°C.

Samples were rinsed in FACS buffer and stained for 30 min at 4°C into FACS buffer with Fc-block and combinations of antibodies to define leukocyte populations. To determine the expression of PD-L1 or CD43 or CX3CR1, samples were also stained with the corresponding antibodies, or *Cx3cr1*^{gfp/+} mice were used. After incubation, samples were washed and resuspended in FACS buffer before analysis. Data were acquired with a FACS Canto II or LSR II (BD Biosciences, USA) and analyzed with FlowJo (USA).

In vivo 4D TPLSM of the cremaster muscle microcirculation

Male mice were immobilized, and the cremaster muscle was carefully exposed while kept moisturized at 37°C during the procedure. Anti-PD-L1 PercP-Cy5.5 antibody was injected in the tail vein (1.5 μ g in 200 μ l of sterile PBS) and allowed to recirculate for 5 min.

For intravital imaging, a Leica TCS SP5II MP (Germany) equipped with a Ti:Sa pulsed laser (Spectra-Physics) tuned at 800 nm was used. Signals deriving from the dye, autofluorescent structures, and second harmonic generation (SHG) of collagen were detected into hybrid diode detectors set as follows: 390 to 420 nm for SHG; 430 to 500 nm for blue autofluorescence; 500 to 590 nm for green autofluorescence; and 600 to 670 nm for PercP-Cy5. Image stacks measuring about 300 to 400 μ m in *xy* and 65 to 85 μ m in *z* (step size, 3 μ m) were acquired over 10 to 12 min at an acquisition rate of 0.03 to 0.05 Hz per stack (depending on the acquired volume; single frame rate, 0.5 to 1 Hz) through a 20 \times 1.00 water dipping objective. 3D stacks were processed in Imaris (Bitplane, Switzerland), denoised with a Gaussian filter (3 \times 3), and automatically z-registered when necessary. PD-L1⁺ cells were segmented according to PercP-Cy5.5 intensity and an average cell diameter of 5 to 8 μ m. Cell tracks were reconstructed choosing a maximal displacement step of 2 μ m between two consecutive time points. Track plots in 3D were created using the "Plot all tracks with a common origin" extension of MATLAB R2016b (MathWorks, USA).

TPLSM of whole-mounted BM

After euthanasia, femurs were collected and prepared for imaging as described previously (36). Stainings were performed on non-permeabilized samples to avoid nonspecific binding to any intracellular antigen. Directly conjugated rat anti-mouse antibodies against the

following antigens were diluted into the blocking solution and incubated overnight at RT in the dark: PD-L1, Gr-1, CD115, CD45.1, and laminin. For Fig. 4C, bones were first incubated overnight at RT using biotinylated rat anti-mouse PD-L1 and primary goat anti-mouse PDGFR β 1, followed by washing and incubation with fluorescently conjugated streptavidin and labeled secondary donkey anti-goat antibody overnight at RT. After staining, bones were washed several times with PBS and embedded into 1.5% agarose gel (in PBS) before imaging.

TPLSM was performed on a Leica SP5II MP sequentially tuned at 800 and 900 nm for optimal excitation. To allow simultaneous collection of different spectra while minimizing color spillover, the hybrid diode detectors were tuned to 380 to 410 nm for bone collagen-derived SHG signal, 420 to 470 nm for Pacific blue, 500 to 550 nm for Alexa Fluor 488/FITC, 600 to 650 nm for Alexa Fluor 594, and 660 to 770 nm for PercP-Cy5.5. Z-stacks (step size, 1 μ m) of 740 μ m \times 740 μ m xy fields of view were collected through a 20 \times 1.00 water dipping objective up to 100- to 150- μ m depth. For each bone, multiple fields of view were acquired in both the epiphysis and diaphysis.

TPLSM of mouse TLOs

After euthanasia, thoracic cavity was exposed, and PAT was detached and kept on ice, washed with PBS, and blocked with PBS with 5% BSA and Fc-block for 2 hours at 4°C. Directly labeled antibodies against PD-L1, CD115, CD3, and B220 were added to the blocking solution, and staining was carried out overnight at 4°C. Samples were washed in PBS and embedded into 1.5% agarose gel for imaging. For Annexin V staining, freshly dissected PAT was immediately incubated into PBS containing Annexin V, Fc-block, and anti-CD3 antibody for 30 min at RT to minimize false-positive signal. After washing, samples were fixed with 4% paraformaldehyde (PFA) at 4°C for 4 hours. TPLSM was performed as described for the whole-mounted BM, and TLOs were defined as B220⁺ and CD3⁺ clusters.

MI surgical model

After anesthesia, a left thoracotomy was performed in the fourth left intercostal space, and the pericardium was incised. MI was induced by permanent ligation of the left anterior descending coronary artery with monofilament nylon 8-0 sutures (Ethicon, USA). The chest wall and skin were closed with 5-0 nylon sutures. After surgery, naloxone (1.2 mg/kg), flumazenil (0.5 mg/kg), and atipamezol (2.5 mg/kg) were injected to reverse anesthesia. Postoperative analgesia (buprenorphine; 0.1 mg/kg) was given for the first 12 hours after surgery. Sham-operated animals had the same surgical protocol without coronary occlusion.

In vivo inhibition of PD-L1

Twenty-four hours post-MI surgery, mice were treated with anti-PD-L1 (10 mg/kg) or immunoglobulin G (IgG) isotype antibody. Euthanasia and harvesting of PAT were performed 48 and 96 hours after treatment, corresponding to days 3 and 5 after MI.

SUPPLEMENTARY MATERIALS

immunology.sciencemag.org/cgi/content/full/4/36/eaar3054/DC1

Materials and Methods

Fig. S1. In silico identification of candidate markers for BM and PB NCMs.

Fig. S2. Anti-PD-L1 antibody is preferable to Cx3cr1^{9p/+} mice to mark circulating NCMs.

Fig. S3. Anti-CD43 antibody does not specifically mark circulating NCMs.

Fig. S4. PD-L1 expression is strongly reduced in *Nr4a1*^{-/-} mice lacking NCMs.

Fig. S5. Kinetics and concentration of the anti-PD-L1 antibody for in vivo labeling of NCMs.

Fig. S6. CD43 does not specifically distinguish NCMs in the BM.

Fig. S7. CMs are the main monocyte subset in physical contact with TZ vessels in the diaphysis, whereas NCMs are in proximity of sinusoids.

Fig. S8. Transfer of purified CMs and BrdU pulse-chase experiment.

Fig. S9. PD-L1 expression is maintained on NCMs under inflammatory conditions, and PD-L1⁺ NCMs are found in TLOs.

Fig. S10. Anti-PD-L1 treatment does not deplete circulating NCMs.

Table S1. Association between the number of PD-L1⁺ cells and vessel subtypes.

Table S2. List of antibodies.

Movie S1. In vivo tracking of patrolling PD-L1⁺ NCMs in the cremaster microcirculation.

Data file S1. List of genes differentially expressed in CMs and NCMs.

Data file S2. Raw data from main figures.

Data file S3. Raw data from supplementary figures.

REFERENCES AND NOTES

1. Feissmann, S. Jung, D. R. Littman, Blood monocytes consist of two principal subsets with distinct migratory properties. *Immunity* **19**, 71–82 (2003).
2. C. Auffray, D. Fogg, M. Garfa, G. Elain, O. Join-Lambert, S. Kayal, S. Sarnacki, A. Cumano, G. Lauvau, F. Geissmann, Monitoring of blood vessels and tissues by a population of monocytes with patrolling behavior. *Science* **317**, 666–670 (2007).
3. L. M. Carlin, E. G. Stamatiaides, C. Auffray, R. N. Hanna, L. Glover, G. Vizcay-Barrena, C. C. Hedrick, H. T. Cook, S. Diebold, F. Geissmann, Nr4a1-dependent Ly6C(low) monocytes monitor endothelial cells and orchestrate their disposal. *Cell* **153**, 362–375 (2013).
4. M. P. Rodero, L. Poupel, P. L. Loyher, P. Hamon, F. Licata, C. Pessel, D. A. Hume, C. Combadière, A. Boissonnas, Immune surveillance of the lung by migrating tissue monocytes. *eLife* **4**, e07847 (2015).
5. C. Auffray, D. K. Fogg, E. Narni-Mancinelli, B. Senechal, C. Trouillet, N. Saederup, J. Leemput, K. Bigot, L. Campisi, M. Abitbol, T. Molina, I. Charo, D. A. Hume, A. Cumano, G. Lauvau, F. Geissmann, CX3CR1⁺ CD115⁺ CD135⁺ common macrophage/DC precursors and the role of CX3CR1 in their response to inflammation. *J. Exp. Med.* **206**, 595–606 (2009).
6. S. Z. Chong, M. Evrard, S. Devi, J. Chen, J. Y. Lim, P. See, Y. Zhang, J. M. Adrover, B. Lee, L. Tan, J. L. Li, K. H. Liong, C. Phua, A. Balachander, A. Boey, D. Liebl, S. M. Tan, J. K. Chan, K. Balabanian, J. E. Harris, M. Bianchini, C. Weber, J. Duchene, J. Lum, M. Poidinger, Q. Chen, L. Renia, C. I. Wang, A. Larbi, G. J. Randolph, W. Wenginger, M. R. Looney, M. F. Krummel, S. K. Biswas, F. Ginhoux, A. Hidalgo, F. Bachelier, L. G. Ng, CXCR4 identifies transitional bone marrow premonocytes that replenish the mature monocyte pool for peripheral responses. *J. Exp. Med.* **213**, 2293–2314 (2016).
7. J. Hettinger, D. M. Richards, J. Hansson, M. M. Barra, A. C. Joschko, J. Krijgsvel, M. Feuerer, Origin of monocytes and macrophages in a committed progenitor. *Nat. Immunol.* **14**, 821–830 (2013).
8. S. Jung, J. Aliberti, P. Graemmel, M. J. Sunshine, G. W. Kreutzberg, A. Sher, D. R. Littman, Analysis of fractalkine receptor CX3CR1 function by targeted deletion and green fluorescent protein reporter gene insertion. *Mol. Cell. Biol.* **20**, 4106–4114 (2000).
9. L. M. Carlin, C. Auffray, F. Geissmann, Measuring intravascular migration of mouse Ly6C(low) monocytes in vivo using intravital microscopy. *Curr. Protoc. Immunol.* **Chapter 14**, Unit. 14.33.1–16 (2013).
10. A. Quintar, S. McArdle, D. Wolf, A. Marki, E. Ehinger, M. Vassallo, J. F. Miller, Z. Mikulski, K. Ley, K. Buscher, Endothelial protective monocyte patrolling in large arteries intensified by western diet and atherosclerosis. *Circ. Res.* **120**, 1789–1799 (2017).
11. M. Evrard, S. Z. Chong, S. Devi, W. K. Chew, B. Lee, M. Poidinger, F. Ginhoux, S. M. Tan, L. G. Ng, Visualization of bone marrow monocyte mobilization using Cx3cr1^{9p/+} Flt3L^{-/-} reporter mouse by multiphoton intravital microscopy. *J. Leukoc. Biol.* **97**, 611–619 (2015).
12. S. Yona, K. W. Kim, Y. Wolf, A. Mildner, D. Varol, M. Breker, D. Strauss-Ayali, S. Viukov, M. Williams, A. Misharin, D. A. Hume, H. Perlman, B. Malissen, E. Zelzer, S. Jung, Fate mapping reveals origins and dynamics of monocytes and tissue macrophages under homeostasis. *Immunity* **38**, 79–91 (2013).
13. A. Mildner, J. Schonheit, A. Giladi, E. David, D. Lara-Astiaso, E. Lorenzo-Vivas, F. Paul, L. Chappell-Maor, J. Priller, A. Leutz, I. Amit, S. Jung, Genomic characterization of murine monocytes reveals C/EBP β transcription factor dependence of Ly6C⁺ cells. *Immunity* **46**, 849–862.e7 (2017).
14. J. Gamrekleshvili, R. Giagnorio, J. Jussofie, O. Soehnlein, J. Duchene, C. G. Briseño, S. K. Ramasamy, K. Krishnasamy, A. Limbourg, T. Kapanadze, C. Ishifune, R. Hinkel, F. Radtke, L. J. Strobl, U. Zimmer-Strobl, L. C. Napp, J. Bauersachs, H. Haller, K. Yasutomo, C. Kupatt, K. M. Murphy, R. H. Adams, C. Weber, F. P. Limbourg, Regulation of monocyte cell fate by blood vessels mediated by Notch signalling. *Nat. Commun.* **7**, 12597 (2016).
15. C. Sunderkötter, T. Nikolic, M. J. Dillon, N. Van Rooijen, M. Stehling, D. A. Drevets, P. J. Leenen, Subpopulations of mouse blood monocytes differ in maturation stage and inflammatory response. *J. Immunol.* **172**, 4410–4417 (2004).
16. B. Becher, A. Schlitzer, J. Chen, F. Mair, H. R. Sumatoh, K. W. Teng, D. Low, C. Ruedl, P. Riccardi-Castagnoli, M. Poidinger, M. Greter, F. Ginhoux, E. W. Newell,

- High-dimensional analysis of the murine myeloid cell system. *Nat. Immunol.* **15**, 1181–1189 (2014).
17. R. N. Hanna, L. M. Carlin, H. G. Hubbeling, D. Nackiewicz, A. M. Green, J. A. Punt, F. Geissmann, C. C. Hedrick, The transcription factor NR4A1 (Nur77) controls bone marrow differentiation and the survival of Ly6C⁺ monocytes. *Nat. Immunol.* **12**, 778–785 (2011).
 18. J. B. Beltman, A. F. Marée, R. J. de Boer, Analysing immune cell migration. *Nat. Rev. Immunol.* **9**, 789–798 (2009).
 19. A. P. Kusumbe, S. K. Ramasamy, T. Itkin, M. A. Mãe, U. H. Langen, C. Betscholtz, T. Lapidot, R. H. Adams, Age-dependent modulation of vascular niches for haematopoietic stem cells. *Nature* **532**, 380–384 (2016).
 20. M. Horckmans, M. Bianchini, D. Santovito, R. T. A. Megens, J. Y. Springael, I. Negri, M. Vacca, M. Di Eusanio, A. Moschetta, C. Weber, J. Duchene, S. Steffens, Pericardial adipose tissue regulates granulopoiesis, fibrosis, and cardiac function after myocardial infarction. *Circulation* **137**, 948–960 (2018).
 21. C. Sun, R. Mezzadra, T. N. Schumacher, Regulation and function of the PD-L1 checkpoint. *Immunity* **48**, 434–452 (2018).
 22. S. Devi, A. Li, C. L. Westhorpe, C. Y. Lo, L. D. Abeynaïke, S. L. Snelgrove, P. Hall, J. D. Ooi, C. G. Sobey, A. R. Kitching, M. J. Hickey, Multiphoton imaging reveals a new leukocyte recruitment paradigm in the glomerulus. *Nat. Med.* **19**, 107–112 (2013).
 23. R. M. Gibbons Johnson, H. Dong, Functional expression of programmed death-ligand 1 (B7-H1) by immune cells and tumor cells. *Front. Immunol.* **8**, 961 (2017).
 24. R. Chèvre, J. M. González-Granado, R. T. Megens, V. Sreeramkumar, C. Silvestre-Roig, P. Molina-Sanchez, C. Weber, O. Soehnlein, A. Hidalgo, V. Andres, High-resolution imaging of intravascular atherogenic inflammation in live mice. *Circ. Res.* **114**, 770–779 (2014).
 25. S. Wantha, J. E. Alard, R. T. Megens, A. M. van der Does, Y. Döring, M. Drechsler, C. T. Pham, M. W. Wang, J. M. Wang, R. L. Gallo, P. von Hundelshausen, L. Lindbom, T. Hackeng, C. Weber, O. Soehnlein, Neutrophil-derived cathelicidin promotes adhesion of classical monocytes. *Circ. Res.* **112**, 792–801 (2013).
 26. M. Acar, K. S. Kocherlakota, M. M. Murphy, J. G. Peyer, H. Oguro, C. N. Inra, C. Jaiyeola, Z. Zhao, K. Luby-Phelps, S. J. Morrison, Deep imaging of bone marrow shows non-dividing stem cells are mainly perisinusoidal. *Nature* **526**, 126–130 (2015).
 27. X. M. Li, Z. Hu, M. L. Jorgenson, W. B. Slayton, High levels of acetylated low-density lipoprotein uptake and low tyrosine kinase with immunoglobulin and epidermal growth factor homology domains-2 (Tie2) promoter activity distinguish sinusoids from other vessel types in murine bone marrow. *Circulation* **120**, 1910–1918 (2009).
 28. K. K. Sivaraj, R. H. Adams, Blood vessel formation and function in bone. *Development* **143**, 2706–2715 (2016).
 29. T. Itkin, S. Gur-Cohen, J. A. Spencer, A. Schajnovitz, S. K. Ramasamy, A. P. Kusumbe, G. Lederger, Y. Jung, I. Milo, M. G. Poulos, A. Kalinkovich, A. Ludin, O. Kollet, G. Shakhar, J. M. Butler, S. Rafii, R. H. Adams, D. T. Scadden, C. P. Lin, T. Lapidot, Distinct bone marrow blood vessels differentially regulate haematopoiesis. *Nature* **532**, 323–328 (2016).
 30. F. Ginhoux, S. Jung, Monocytes and macrophages: Developmental pathways and tissue homeostasis. *Nat. Rev. Immunol.* **14**, 392–404 (2014).
 31. M. C. Dieu-Nosjean, J. Goc, N. A. Giraldo, C. Sautès-Fridman, W. H. Fridman, Tertiary lymphoid structures in cancer and beyond. *Trends Immunol.* **35**, 571–580 (2014).
 32. R. Jitschin, M. Braun, M. Büttner, K. Dettmer-Wilde, J. Bricks, J. Berger, M. J. Eckart, S. W. Krause, P. J. Oefner, K. Le Blanc, A. Mackensen, D. Mougiakakos, CLL-cells induce IDO^{hi} CD14⁺HLA-DR^{lo} myeloid-derived suppressor cells that inhibit T-cell responses and promote T_{Regs}. *Blood* **124**, 750–760 (2014).
 33. F. Haderk, R. Schulz, M. Iskar, L. L. Cid, T. Worst, K. V. Willmund, A. Schulz, U. Warnken, J. Seiler, A. Benner, M. Nessling, T. Zenz, M. Göbel, J. Dürig, S. Diederichs, J. Paggetti, E. Moussay, S. Stilgenbauer, M. Zapatka, P. Lichter, M. Seiffert, Tumor-derived exosomes modulate PD-L1 expression in monocytes. *Sci. Immunol.* **2**, eaah5509 (2017).
 34. J. Kapelleris, A. Kulasinghe, M. E. Warkiani, I. Vela, L. Kenny, K. O'Byrne, C. Punyadeera, The prognostic role of circulating tumor cells (CTCs) in lung cancer. *Front. Oncol.* **8**, 311 (2018).
 35. C. Reeps, J. Pelisek, S. Seidl, T. Schuster, A. Zimmermann, A. Kuehn, H. H. Eckstein, Inflammatory infiltrates and neovessels are relevant sources of MMPs in abdominal aortic aneurysm wall. *Pathobiology* **76**, 243–252 (2009).
 36. J. Duchene, I. Novitzky-Basso, A. Thiriot, M. Casanova-Acebes, M. Bianchini, S. L. Etheridge, E. Hub, K. Nitz, K. Artinger, K. Eller, J. Caamaño, T. Rüllicke, P. Moss, R. T. A. Megens, U. H. von Andrian, A. Hidalgo, C. Weber, A. Rot, Atypical chemokine receptor 1 on nucleated erythroid cells regulates hematopoiesis. *Nat. Immunol.* **18**, 753–761 (2017).

Funding: The present work was supported by the Deutsche Forschungsgemeinschaft grants SFB1123 Z1 (to R.T.A.M.), A1 (to C.W.), A2 (to P.v.H.), A5 (to N.G.), A10 (to J.D. and C.W.), and B9 (to S.S.); MO 3054/1-1 (to S.K.M.); INST409/97-1FUGG and INST409/150-1FUGG (to C.W. and R.T.A.M.); and European Research Council grant ERC_AdG⁶92511 (to C.W.). **Author contributions:** M.B., J.D., C.W., and R.T.A.M. designed the research and wrote the manuscript. M.B., J.D., M.J.S., M.E., H.W., M.A., S.K.M., M.H., M.L., X.B., and R.T.A.M. performed the experiments. M.B., J.D., D.S., and R.T.A.M. analyzed the data and performed the statistical analysis. P.v.H., D.A., N.G., A.H., J.P., L.G.N., and S.S. provided consumables, samples, and intellectual input. J.D., C.W., and R.T.A.M. provided funds. **Competing interests:** The authors declare that they have no competing interests. **Data and materials availability:** All data needed to evaluate the conclusions in the paper are present in the paper or the Supplementary Materials. All reagents and mouse strains are commercially available, as indicated in the manuscript.

Submitted 8 November 2017
Resubmitted 1 February 2019
Accepted 20 May 2019
Published 21 June 2019
10.1126/sciimmunol.aar3054

Citation: M. Bianchini, J. Duchêne, D. Santovito, M. J. Schloss, M. Evrard, H. Winkels, M. Aslani, S. K. Mohanta, M. Horckmans, X. Blanchet, M. Lacy, P. von Hundelshausen, D. Atzler, A. Habenicht, N. Gerdes, J. Pelisek, L. G. Ng, S. Steffens, C. Weber, R. T. A. Megens, PD-L1 expression on nonclassical monocytes reveals their origin and immunoregulatory function. *Sci. Immunol.* **4**, eaar3054 (2019).

PD-L1 expression on nonclassical monocytes reveals their origin and immunoregulatory function

Mariaelvy Bianchini, Johan Duchêne, Donato Santovito, Maximilian J. Schloss, Maximilien Evrard, Holger Winkels, Maria Aslani, Sarajo K. Mohanta, Michael Horckmans, Xavier Blanchet, Michael Lacy, Philipp von Hundelshausen, Dorothee Atzler, Andreas Habenicht, Norbert Gerdes, Jaroslav Pelisek, Lai Guan Ng, Sabine Steffens, Christian Weber and Remco T. A. Megens

Sci. Immunol. 4, eaar3054.

DOI: 10.1126/sciimmunol.aar3054

Nonclassical Monocyte Marker

Nonclassical monocytes (NCMs) are a subset of monocytes that act as sentinels in the skin endothelium and lung microvasculature. The origin of NCMs is not well understood, and Bianchini *et al.* now identify the immune checkpoint molecule PD-L1 as a marker that can track NCMs. Using two-photon microscopy, PD-L1⁺ NCMs could be tracked within the bone marrow, and contact with endosteal vessels was required for conversion from classical monocytes to NCMs. Under inflammatory conditions, PD-L1⁺ NCMs were found in tertiary lymphoid organs (TLOs), and expression of PD-L1 by NCMs regulated T cell survival in TLOs. Together, these findings reveal PD-L1 as a valuable tool for studying the origin and functions of NCMs.

ARTICLE TOOLS

<http://immunology.sciencemag.org/content/4/36/eaar3054>

SUPPLEMENTARY MATERIALS

<http://immunology.sciencemag.org/content/suppl/2019/06/17/4.36.eaar3054.DC1>

REFERENCES

This article cites 36 articles, 13 of which you can access for free
<http://immunology.sciencemag.org/content/4/36/eaar3054#BIBL>

Use of this article is subject to the [Terms of Service](#)